Reduction of the effective shear viscosity in polymer solutions due to cross-flow migration in micro-channels: effective viscosity models based on DPD simulations

T. L. Palmer[a,b], G. Baardsen[d,c], R. Skartlien[c,b,e]

[a] *University of Stavanger, P.O. Box 8600, N-4036 Stavanger, Norway*
[b] *IOR Centre of Norway*
[c] *Institute for Energy Technology, P.O. Box 40, N-2027 Kjeller, Norway*
[d] *Centre for Theoretical and Computational Chemistry, Department of Chemistry, University of Oslo, P.O. Box 1033 Blindern, N-0315 Oslo, Norway*
[e] *Dept. of Chemical Engineering, Ugelstad Lab., NTNU, N-7491 Trondheim, Norway*

Abstract

Molecular dynamics simulations (Dissipative Particle Dynamics - DPD) were developed and used to quantify wall-normal migration of polymer chains in microchannel Poseuille flow. Crossflow migration due to viscous interaction with the walls results in lowered polymer concentration near the channel walls. A larger fraction of the total flow volume becomes depleted of polymer when the channel width h decreases into the sub-micron range, significantly reducing the effective viscosity. The effective viscosity was quantified in terms of channel width and Weissenberg number Wi, for 5% polymer volume fraction in water. Algebraic models for the depletion width $\delta(Wi, h)$ and effective viscosity $\mu_e(\delta/h, Wi)$ were developed, based on the hydrodynamic theory of Ma and Graham and our simulation results. The depletion width model can be applied to longer polymer chains after a re-tuning of

Email address: teresa.palmer@ife.no (T. L. Palmer)

the polymer persistence length and corresponding potential/thermal energy ratio.

Keywords: polymer migration, polymer rheology, effective viscosity, porous media, DPD

---

1. Introduction

Polymer solutions are used in many applications, from drag reducers in turbulent pipe flow [1], to viscosity boosters in injected water during oil recovery [2, 3, 4]. A transition from capillary fingering to a stable invading water front can be achieved in an oil reservoir when the viscosity of the injected water is increased by adding polymer [5]. However, many polymer solutions, including partially hydrolyzed polyacrylamide (HPAM), can exhibit lowered effective viscosity due to lowered polymer concentration near the mineral surface due to cross-flow migration. This depleted layer has low viscosity, and acts as a lubricating layer, increasing the volumetric flux of liquid for the same pressure gradient. Technology developments for DNA research are also concerned with the same type of migration effects in capillary tubes and narrow channels [6, 7].

In essence, the near-wall depletion layer develops due to hydrodynamic migration of flow-aligned polymer chains towards the central parts of the flow channel [8], or due to direct steric interaction between polymer segments and the confining wall [9]. The reduction of effective viscosity becomes significant for narrower channels in the micron range (e.g., sandstone reservoirs), because the depleted volume becomes a larger fraction of the total fluid volume. A reduction of the effective viscosity by a factor of at least two is found

experimentally for HPAM flow in channels with plane walls when the channel width is reduced from ten to one micron [10].

Migration and depletion is a fundamental mechanism that is likely to occur also in the complex geometry of reservoir rocks [2, 3, 4], although modifications (e.g., due to more complex steam lines) will be present. It is therefore expected that water breakthrough may occur with higher probability than anticipated, since the effective viscosity is reduced compared to a polymer solution with homogeneously distributed polymer in the pore structure.

The migration and wall-polymer interaction mechanisms depend on the ionic strength of the solvent (including salinity variations) when the polymer contains charged groups. Ions may shield the polymer charges, and therefore reduce the polymer extension, which again can influence the depletion layer width. Adsorption of polymer on the mineral may modify the depletion mechanism, depending on the properties of the adsorbed layer in terms of hydrodynamic roughness. The adsorbed surface density is also influenced by the ionic composition of the solvent and the chemical constitution of the given mineral [11].

We used resolved molecular simulations of the DPD-type (Dissipative Particle Dynamics) [12]. This approach preserves viscoelastic and shear thinning rheologies of the polymer solution and the viscous hydrodynamic coupling to the confining walls, and between different polymers. We used simple channel geometry for now, although the simulation code that was developed can handle both complex geometries and adsorption.

Since the mechanisms that contribute to migration are numerous and complex, it is not surprising that models for polymer migration tend to be

less general than what is usually needed for application. Confined polymers between flat walls without flow offer analytic treatments [9, 13, 14], as does simplified dumbbell models in shear flow [15]. For more realistic cases of migration with long polymer chains, there are a number of empirical results from experiments [7, 10], DPD simulations [16, 17, 18, 19, 20] and Brownian and molecular dynamics simulations [6, 21, 22] that qualitatively describe the depletion layer behavior within the given parameter range. Ready-to-apply models for the depletion layer thickness δ as function of the Weissenberg number Wi, the channel width h, ion contents/salinity, and adsorption properties are still lacking as far as we are aware. One goal of the current study is to derive a phenomenological relation $\delta(Wi, h)$ based on the simulations results and knowledge already obtained in the literature.

For low Wi (the Newtonian regime) the polymers are not extended significantly by shear, and it is the radius of gyration R_g which is the relevant polymer size, and R_g/h becomes the controlling parameter for δ. The polymers tend to stay coiled up if the channel width is large enough, and the polymers interact sterically with the wall, generating a depleted layer if there is no adsorption [14]. It is then reasonable to assume that a slight stretching of the polymers for increasing Wi brings them closer to the wall [23, 24]. The flow-aligned length is increased ($R_{||} > R_g$), and the relevant size scale is now the smaller extension perpendicular to the wall $R_\perp < R_g$, and the polymers can get closer to the wall. Indeed, Fedosov and coworkers [19] used DPD simulations to study polymer migration in a moderately confined regime of channel widths $h = (3 - 8)R_g$ in Poseuille flow and found a reduction of the depletion layer thickness δ for increased Wi. Similarly, de Pablo and

coworkers [23] found that δ diminished with increasing shear rates at low Wi. However, δ reached a minimum at a Weissenberg number between 10 and 100, before it increased again at higher Wi.

For higher Wi in the shear thinning regime, it has been argued that hydrodynamic viscous interaction with the wall results in migration away from the wall, and the polymers may migrate further into the core flow with increasing shear rates [15]. A simplified dumbbell model for the polymer allows for a rigorous calculation of the depletion layer thickness δ if Stokes flow interaction with a single wall is assumed. With this basis, δ scales asymptotically as $Wi^{2/3}$ for large Wi [15]. This type of migration increases for increasing polymer/dumbbell length, and vanishes in very narrow channels due to a cancellation between the two walls [8]. Molecular dynamics simulations in Couette flow show that the depletion layer grows with increased Wi as predicted for hydrodynamic migration [22], and the same behavior was found in Poseuille flow with DPD simulations [20]. With increasing depletion layer thickness, we expect that the shear thinning effect is amplified, giving a steeper slope of the effective viscosity curve as function of Wi.

The depletion layer thickness δ increases with channel width h in Couette flow [22] and in Poseuille flow [19], with an apparent asymptotic behavior (with the limit $\delta \simeq R_g$). Near-wall depletion implies a concentration build-up in the core flow that is larger for narrower channels, implying a self-regulating effect from gradient diffusion back towards the walls. Polymer diffusion smooths out density gradients, but the diffusivity depends on polymer elongation [19]. Highly elongated polymers do not diffuse as efficiently perpendicular to their stretching direction and the wall-normal diffusive fluxes

are therefore reduced with increased Weissenberg number. Another important effect is that the depletion layer tends to thin for increasing polymer concentration due to polymer-polymer interaction [9, 20], suggesting that depletion effects can be more important for dilute solutions (of the type used for water injection).

2. Polymer DPD simulator with parallel processing

We have developed a 3D DPD (Dissipative Particle Dynamics) simulator for parallel processing, tailored to polymer flow in arbitrary wall geometries. With DPD, one can identify the polymer migration mechanisms in any geometry, and evaluate their effect on the effective viscoelastic rheology. Adsorption and salinity effects can be analyzed by choosing the appropriate wall-polymer, and polymer-polymer interaction parameters, respectively.

2.1. Basic DPD framework and polymer visco-elasticity

DPD is a Lagrangian method, where the molecular structure is modelled to some level of coarse graining [12, 19, 20]. In a Eulerian continuum representation, one must solve a transport equation for the hydrodynamic stress tensor that incorporates the associated history effects of the viscoelastic polymers (e.g., the Oldroyd model). This is not necessary for the more direct DPD approach since the viscoelastic history effects emerge via the intra-molecular forces.

A detailed description of DPD can be found in the now extensive literature [25, 26, 27, 28, 29, 12]. A coarse grained DPD polymer model consists of a number of linked beads that each represent a limited number of atoms. The solvent (water) is modelled as single beads that each represent a number of

water molecules (here, three molecules). The positions of the beads were integrated over time using the velocity-Verlet method [30, 31, 32], and a suitable force model $\mathbf{F}_{ij}^{C}$ for the electrostatic/van der Waals forces between any given pair of beads (i and j). This *conservative* force is derived from an interaction potential

$$U(r_{ij}) = a_{ij}\mathcal{U}(r_{ij}) \tag{1}$$

with a given functional form $\mathcal{U}$. The distance vector $\mathbf{r}_{ij} = \mathbf{r}_i - \mathbf{r}_j$ is defined by the position vectors $\mathbf{r}_i$ and $\mathbf{r}_j$ of particles i and j respectively, and the length of the distance vector is $r_{ij} = |\mathbf{r}_{ij}|$. This potential represents a simple approximation to the coarse grained potential obtained by averaging over the underlying atomic structure and the associated van der Waals or Lennard-Jones type potentials. The conservative forces are repulsive in DPD, so that increasing a_{ij} corresponds to increased repulsion. The interaction strengths a_{ij} are given as input.

A harmonic "spring-force" is added between polymer beads to keep the chains intact, and this force give rise to fluid elasticity. In our parallelized implementation of the DPD algorithm, it was numerically convenient to restrict the bond interaction to have a fixed, finite range. The bond breaks if the distance between the beads becomes larger than R_B [33],

$$\mathbf{F}^{H}(\mathbf{r}_{ij}) = \begin{cases} -C\,(r_{ij} - r_0)\,\mathbf{u}_{ij}, & \text{if } r_{ij} \leq R_B \\ 0, & \text{else,} \end{cases} \tag{2}$$

where $\mathbf{u}_{ij} = \mathbf{r}_{ij}/r_{ij}$ is the normalized distance vector, C is the strength of the interaction and we chose $r_0 = 1.0$ as the equilibrium distance between two polymer beads (normalized to the characteristic DPD scale $r_c = 0.64 \times 10^{-9}\ m$), and $R_B = 2.0$. A high value of $C = 400$ was chosen to prevent

polymer breakup. We confirmed that less than 1% of the bonds were broken for the longer chains with bead numbers $N \geq 60$.

The relative importance of polymer deformation due to viscous hydrodynamic coupling along the polymer chain versus diffusive motion, is controlled by the Schmidt number. It is essential to have higher Schmidt numbers ($Sc \gg 1$) to achieve realistic polymer migration effects [17, 20, 34]. We adjusted the DPD parameters to achieve $Sc = 600$ (Appendix A).

2.2. Parallel algorithms

We use an MPI-standard library for parallel processing [35, 36]. MPI applications can be run in parallel both on off-the-shelf workstations and on distributed computing systems. Different approaches for parallelization of MD and DPD algorithms have been discussed in the literature [37, 38, 39, 40, 41, 42, 43, 32]. The domain-decomposition method (in which different processors consider different space domains) is more efficient for large systems than atomic- and force-decomposition techniques [39]. Therefore, we chose to parallelize our DPD program using a domain-decomposition method. We used the parallel linked cell-list approach, which was first introduced for MD simulations [37] and later generalized to DPD [42]. The parallel linked-cell list algorithm [37, 42] combines linked cell lists [44] (which give linear scaling for short-range interactions) with domain-decomposition parallelization. In the parallel linked-cell list algorithm, the simulation domain is divided into boxes of equal size, each associated with a different processor. Each processor domain is divided into smaller boxes that are used for the linked-cell list algorithm. Following [39, 42], we chose processor configurations with minimal interface areas to minimize the communication between processors.

To calculate nonbonded forces between beads in different processor domains, it is necessary to copy particle data of beads that are within the cutoff radius R_c from a certain processor domain. The copying of nonbonded bead data across processor domains was implemented using ghost cells [37, 42]. For the processing of intra-bead polymer forces, we used large arrays containing relations between global and local particle indices [41], and an option for using shorter time steps (Appendix B).

2.3. No-slip wall boundary conditions for general geometries

The walls were modelled using non-moving wall beads [20]. The wall beads interact with fluid beads through both viscous and conservative forces, as any DPD bead. It is essential to have no-slip boundary conditions when measuring the effective viscosity in the simulations. To obtain this, the fluid beads that come close to the wall are assigned a zero-mean velocity. The random velocity components were drawn from a Maxwell-Boltzmann distribution at the kinetic temperature of the system [45, 46]. When a fluid or polymer bead is closer than a given reflection radius R_w from a wall bead, the fluid bead is assigned a new velocity outwards from the wall surface with an arbitrary direction in the half space defined by the normal vector $\mathbf{n}$ to a smooth mathematical surface that encloses the spatial domain of the wall beads. This approach provides an entirely general treatment for any wall geometry and topology, and emulates a wall with the given kinetic temperature, without having to treat moving or vibrating wall beads [45].

The reflection distance R_w is the radial distance from a wall bead where reflection occurs. The wall beads are placed at random positions in the wall volume, and to avoid "holes" where fluid beads can enter, R_w must be larger

than the average wall bead separation so that the radii from neighboring beads overlap with high probability. We chose a reflection radius of

$$R_w = 0.25, \tag{3}$$

normalized to the DPD length unit r_c. The cutoff radius for the conservative force interactions between fluid and wall beads was set at

$$R_c(wall) = 1.25, \tag{4}$$

and this has to be larger than R_w for wall interaction to occur before reflection happens. The cutoff radius of the forces between the beads in the whole fluid domain was set to $R_c = 1.0$.

To obtain a no-slip condition with sufficient accuracy, a wall bead number density of 4 times the fluid density was implemented [20]. A corresponding reduction of the wall interaction parameter by a factor of 1/4 was used to provide constant fluid density also in the near-wall region.

2.4. Tuning the interaction potentials

The interaction parameters a_{ij} were tuned to obtain the overall solubility behavior of HPAM, and the parameter values were comparable in magnitude to those derived from Flory-Huggins theory [12]. Test runs were carried out to provide homogeneous polymer solutions without phase separation or segregation of the polymer strands into a separate phase. Furthermore, the wall interaction parameters were adjusted to obtain a neutral, non-adsorbing wall.

The a_{ww} parameter is the water - water coupling, and $a_{ww} = 25$ was chosen to match the compressibility of water [12]. For the polymer to be

soluble in water, we also had to set $a_{pp} > a_{wp}$, which provides extended polymer chains. The effect of polymer on viscosity depends on the polymer-water interaction parameter, with more response for higher a_{wp}. However, if a_{wp} is higher than a_{pp} the polymer becomes insoluble, and separates out into polymer clusters. The parameters that we found to be optimal were

$$a_{ij} = \begin{pmatrix} & w & p & s \\ w & 25 & 50 & 25 \\ p & .. & 100 & 50 \\ s & .. & .. & .. \end{pmatrix}, \tag{5}$$

where w, p, s, stand for water, polymer, and wall (substrate) beads, respectively. Setting $a_{wp} > 50$ gave an enhanced viscous response, but resulted in reduced solubility of the polymer, even when $a_{pp} > a_{wp}$. We found the requirement $a_{pp} > 75$ for the polymer to be fully soluble in the water, and $a_{pp} = 100$ was chosen.

Increasing a_{pp} increases the intra-bead repulsion in the polymer chain and increases the radius of gyration R_g, and would mimic smaller ionic concentration (lowered salinity) in the solvent. The viscosity of the polymer solution increased with increasing a_{pp}, because the more extended polymer chains give larger contact area between the polymer and the water. In the current work, we use a neutral wall (no polymer adsorption and no net repulsion), by setting $a_{ps} = a_{wp}$.

2.5. Polymer concentration and chain length

As a reference case, we used a 1000 ppm (mass fraction) solution of polymer in water, that represents a typical case of HPAM injection. We match

the total length of polymer chain per volume of water to obtain the correct surface area between the polymer chains and the water per volume unit, and hence the stress coupling between the water and the polymers should be of the correct magnitude. Unfortunately, the domain size in molecular simulations is too small to span the typical polymer chain lengths of HPAM. This is because larger volumes would increase the number of solvent molecules to a level (tens of millions) were the computations would be intractable.

We were still able to make DPD models of polymer chains that were long enough to obtain a polymer relaxation time that gives shear thinning in a range of shear rates similar to that of HPAM. Shear thinning occurs at a Weissenberg number near unity and above, $Wi = \lambda\dot{\gamma} \geq 1$. The extensional relaxation time λ of synthetic HPAM and organic polymer chains is on the order of 0.1 s [3], and these polymer solutions are therefore shear thinning above a strain rate of about $\dot{\gamma} = 10\ s^{-1}$.

By assuming non-degraded HPAM molecules of mass $m_p = 4 \times 10^6\ Da$, the polymer length is about $L_p = 10\ \mu m$ [47]. The polymer mass density in solution is $\rho_p = 1000\ ppm = 10^{-3} gm/cm^3$. We match the length of polymer per volume,

$$l_v = \frac{\rho_p L_p}{m_p}, \tag{6}$$

and this criterion gives a volume fraction of polymer beads in the DPD simulations of $\phi_p = 5\%$, when the equilibrium bead separation is comparable to the DPD length unit of $r_c = 0.64 \times 10^{-9} m$.

We tested the effect of polymer chain length on the effective viscosity, velocity profile, and concentration profile, with the number of beads in the range $N \in [10, 120]$. Convergent behavior was obtained for chain lengths

$N > 60$. Polymers of length up to $N = 120$ were tested and we found essentially the same behavior as for $N = 60$, and a moderate chain length of $60 r_c r_0 \simeq 4 \times 10^{-2}\ \mu m$ is then our "default" value used for most of the simulations. We also show results for $N = 20$ for comparison.

3. Rheology setup for Poseuille flow

3.1. Effective viscosity measurement

The simulations were set up for Poseuille flow between flat walls, with varying wall distance h. The boundary conditions were periodic in the spanwise and flow-aligned directions. The length of the domain size in the flow direction was 40 and 80 DPD units (of $r_c = 0.64 \times 10^{-9} m$) for $N = 20$ and $N = 60$ respectively, to avoid wrap-around effects of the polymer chains due to the periodic boundary conditions in the flow-aligned direction. The main limitation on the domain size was the number of water molecules, which were in the range $(0.015 - 1.1) \times 10^6$ beads, requiring 2-3 days of computational time on 12 microprocessors for the larger simulations. We used channel widths in the range $h \in [4, 154]$ nm. The largest widths were comparable to the smaller channel widths used in the experiments of Cuenca and Bodiguel [10]. An example with $h = 38$ nm is shown in Figure 1, where the depletion layer is clearly visible.

A body force G was added to emulate the effect of a uniform pressure gradient in the flow direction. The effective viscosity is defined by

$$\mu_e = \frac{h^2}{12} \frac{G}{U}, \tag{7}$$

where U is the average value of the fluid velocity profile (volumetric flux per cross sectional area) and the channel width is h. The effective viscosity

defined in this manner reduces to the fluid viscosity for purely Newtonian fluids, and for polymer Carreau fluids if the shear rate is low enough to remain in the upper Newtonian regime (Appendix C).

To determine the effective viscosity, the velocity profile $u(y)$ was integrated to obtain the average velocity U. The layer of DPD water beads near the no-slip wall were essentially non-moving, giving an effectively narrower channel, and is was necessary to replace the channel width h with $(h - \epsilon)$ in the calculation of the effective viscosity, where $\epsilon \simeq 0.5$ is a fraction of the bead radius.

The simulations were run to steady state after imposing a Newtonian velocity profile. Time averaging was then performed over the solvent and polymer bead velocities. The polymer bead number density was measured in suitable bins Δy in the wall normal direction y. The fluid velocity profile $u(y)$ and polymer concentration profile $c(y)$ could then be estimated. The depletion layer thickness δ was defined as the distance from the wall where the polymer concentration c is equal to its half-value defined by

$$c(\delta) = \frac{1}{2}\langle c(y)\rangle \tag{8}$$

where averaging $\langle..\rangle$ was performed over the full volume of the channel. To estimate the concentration profiles, we used the polymer bead number density, not the center of mass density of the polymer chains [19, 20]. The center of mass density can be misleading close to the wall, giving the appearance of full depletion where in reality the beads may interact directly with the wall.

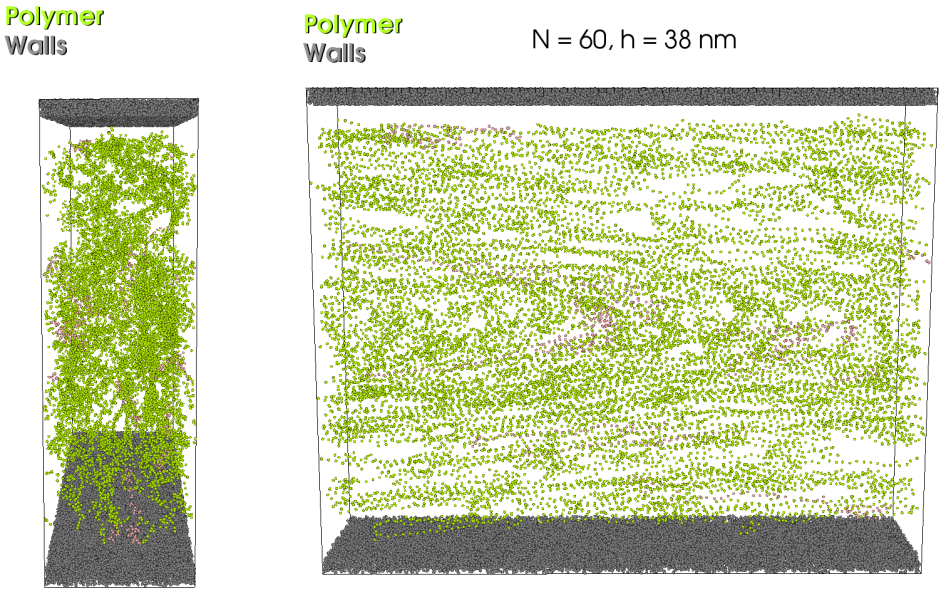

Figure 1: Visualization of the polymer distribution for $h = 38$ nm, $N = 60$, and $Wi = 1.5$. Left: Font view in the flow aligned direction. Right: Side view where the flow is directed to the right. A few polymer strands are colored in pink. The depletion layer is visible as the void near the upper wall. The visualization was generated using the freeware VISIT.

3.2. Weissenberg number constraints

For shear thinning polymer solutions, both the bulk and the effective viscosities decrease with the Weissenberg number (normalized shear rate). We will study the variation of the effective viscosity with varying channel width h, and to separate out this effect one must keep the channel-averaged Weissenberg number

$$Wi = \langle\dot{\gamma}\rangle\lambda \tag{9}$$

at a constant value. The average strain rate

$$\langle\dot{\gamma}\rangle = \frac{1}{h/2}\int_{-h/2}^{0}\partial_y u(y)dy = \frac{u(0)}{h/2} \tag{10}$$

was kept constant by adjusting the velocity $u(0)$ in the center of the channel. This is again controlled by the body force G (equivalent to the pressure gradient). A constant wall shear stress

$$\tau_w = Gh/2, \tag{11}$$

provided an initial estimate for the driving force G when h was varied.

A number of Wi values were chosen in the range $0.5 - 10$. The relaxation time λ of the DPD polymers was defined by the exponential relaxation time from an extended state to a contracted equilibrium state. The end-to-end distance followed approximately the exponential

$$\Delta R \simeq R_0(N) \exp(-t/\lambda(N)), \tag{12}$$

where R_0 and λ are functions of chain length N in terms of the number of beads. Exponential fits to the data produced the needed relaxation times.

4. Simulation results

In this section, we summarize the simulation data in terms of the response of the effective viscosity and depletion layer thickness δ to varying channel height h and Weissenberg number Wi.

4.1. Effective viscosity

Figure 2 shows the relative effective viscosity $\mu_e^* = \mu_e^0/\mu_w$ (where μ_w is the water viscosity) as function of Wi for two channel widths (13 and 38 nm). For a pure power law fluid or a Carreau fluid in the shear thinning regime (Appendix C), we expect the scaling $\mu_e^* \sim \mu_0^*(Wi)^{n-1}$ where n is a constant. Thus, the data reveals an approximate straight line in the shear

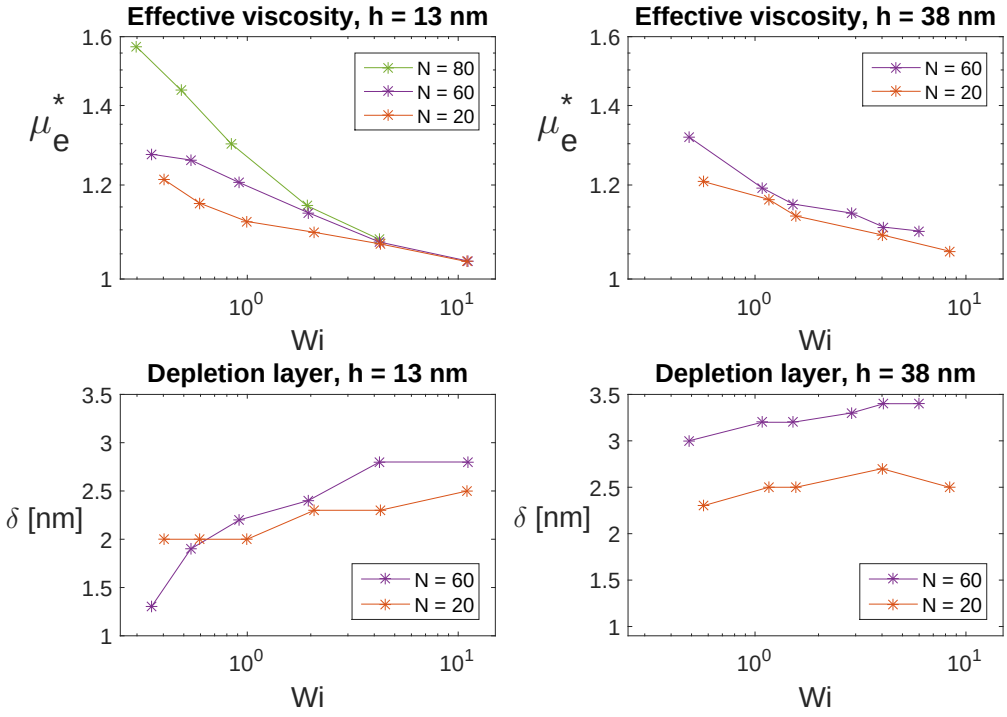

Figure 2: normalized effective viscosity μ_e^* and depletion layer thickness as δ function of Weissenberg number Wi. Left: narrow channel h =13 nm. Right: wider channel h =38 nm. The viscosity is strongly shear thinning, due to the intrinsic shear thinning rheology and increasing depletion layer thickness δ with Wi. The depletion layer δ tends to increase with Wi and channel width h.

thinning regime, where $\log(\mu_e^*) \simeq \log(\mu_0^*) - (1-n)\log(Wi)$. We note that depletion layer effects adds on to the intrinsic shear thinning behavior of the fluid. The slope of the effective viscosity is then steeper with a depletion layer. The depletion layer δ tends to increase with Wi (lower panels), as we will discuss in more detail later. For very high Wi, the viscosity in the core flow is reduced by shear thinning and the viscosity contrast between water and the core flow is lowered, and hence the presence of a depletion layer is

less important.

The effective viscosity from the simulations increases with chain length N in accordance with known polymer behavior (upper panels). However, the viscosity increases less for the higher Weissenberg numbers. The reason for this is that the polymers are stretched out more for higher Wi, and the viscosity does not vary much with chain length in that case since the total chain length per volume solvent is the same in the simulations.

From the data, is it clear that the effect of the chain length on the viscosity is larger than the depletion layer effect: the longer chains give higher viscosity although the depletion layer grows with longer chains.

4.2. Depletion layer effects on the effective viscosity

The variation of the effective viscosity and depletion layer as function of channel width h, is shown in Figure 3 for two Weissenberg numbers (1.5 and 4). From Figure 2, the high Wi represents the transition to the lower Newtonian regime, while the low Wi represents the strongly shear thinning regime. At high Wi we may expect that the influence from depletion is smaller since the viscosity contrast between the depleted layer and the core flow is smaller.

A very important effect on the effective viscosity is that the depletion layer grows less than a linear function of h such that the depleted volume fraction δ/h decreases with increasing h (middle panels), and this is the important parameter that controls the effective viscosity (right hand panels). For large volume fraction δ/h of the depleted layer, the effective viscosity is reduced significantly and this effect is stronger for the narrower channels. Here, the depletion layer thickness becomes a good fraction of the channel

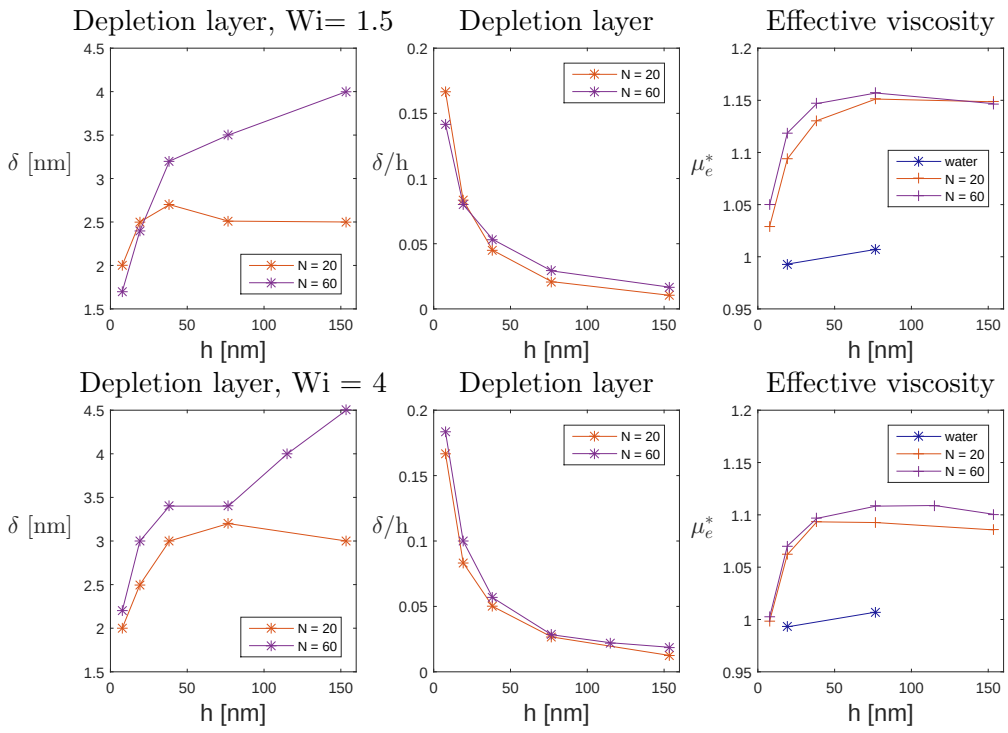

Figure 3: Depletion layer thickness δ, and normalized effective viscosity μ_e^* as function of channel width h.

width. A more gradual increase of δ/h occurs for the wider channels, and the increase of the effective viscosity with h is smaller, due to the relatively thinner depletion layer. The shear thinning effect is more visible for the larger h where it is seen that the effective viscosity is lower for the higher Wi (right hand panels).

Cuenca and Bodiguel [10] found relatively large reductions in effective viscosity with reduced channel width in the sub-micron range for HPAM polymer. This is also the behavior we find in the simulations, where $\delta/h \simeq 0.2$ for the narrower channels around 10 nm, and drops to about $\delta/h \simeq 0.05$ for

widths of 40 nm (Figure 3). This is characteristic for both Weissenberg numbers.

The depletion layer grows with h for the longer chain $N = 60$ (Figure 3 left hand panels). The shorter chain shows a different behavior where the growth stops at smaller h. This is in fact expected as we will discuss later in the modelling section. The depletion layer thickness δ increases as function of Weissenberg number as well (Figure 2). The main physical mechanisms behind the formation of the depletion layer is hydrodynamic migration away from the walls, and an opposing gradient diffusion back towards the walls [15]. The drift away from the walls increases with Wi, and is balanced by back-diffusion when the concentration builds up in the in the core volume of channel. This is in line with earlier findings where increased concentration of polymer reduces the depletion layer thickness [22].

Two confinement effects are of importance when the channel width is reduced. First, the forces that generate migration tends to cancel between the two walls, reducing the migration effect [15], and the concentration builds up faster in the channel for increasing migration flux (increasing Wi). This limits the depletion layer thickness for narrow channels in line with Figure 2 (in the lower panels, even though the data are sparse), and with Figure 3. These ingredients will be incorporated in the depletion layer model developed below.

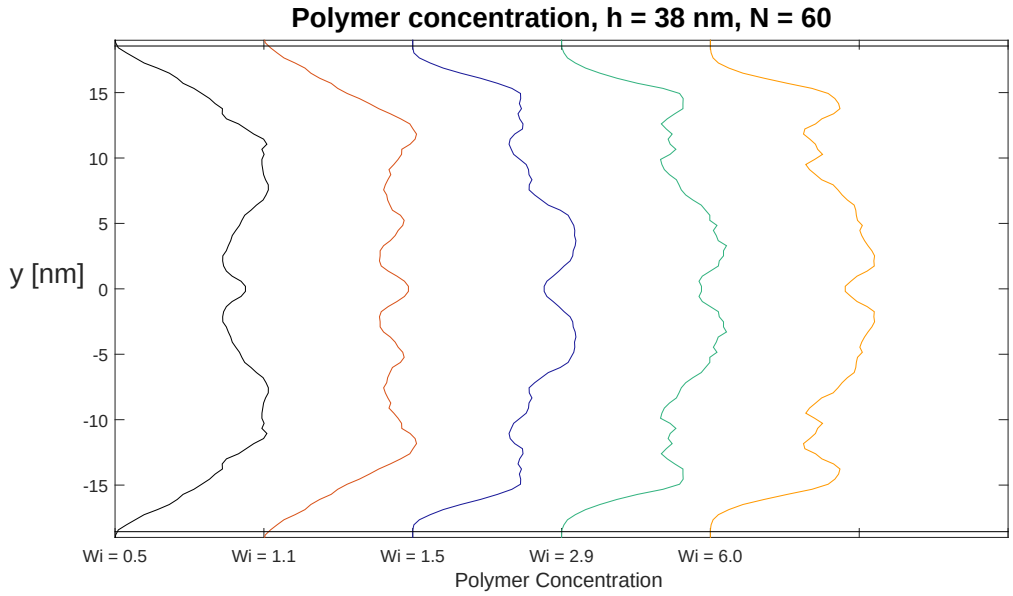

Figure 4: Concentration profiles as function of Wi for $h = 38$ nm. The horizontal lines mark the distance to the wall where direct collisions (steric interaction) with the wall begin to occur with high probability. The depletion layer thickness is larger, indicating hydrodynamic rather than steric interaction.

4.3. Concentration profiles

Concentration profiles for $h = 38$ nm and $N = 60$ are shown in Figure 4 for a set of Weissenberg numbers. To reduce the noise level, we performed time averaging over the full dataset after a steady state situation was established, and ensemble averaging was performed in some cases over different simulation runs. Furthermore, the profiles were mirrored and added to reduce noise further (due to symmetry).

The horizontal lines mark the distance to the wall where direct collisions with the wall begin to occur with high probability at the interaction distance $R_c(wall) = 1.25$ (in DPD units) for the conservative force. It is clear that, at

least for the higher Weissenberg numbers, that the polymers do not interact directly by collisions with the wall, so that hydrodynamic migration away from the wall is the likely migration mechanism. The diffusive flux towards the walls balances the migration fluxes away from the walls [15].

The profiles show a tendency of a characteristic enhanced concentration on the shoulders of the concentration profile (also found by other autors [8]). The polymer elongation is controlled by the local shear rate so that high shear rates may reduce the diffusivity and cause a pile-up of polymer that were originally in the core region, into the high shear regions, generating the "volcano" shape. Long, elongated polymers at high Weissenberg numbers may also tend to be "locked in place" by the shear at a certain distance to the wall due to the strongly reduced diffusivity. For this reason we performed several runs in some cases with statistically independent initial conditions.

5. Effective viscosity models

A goal of this work was to develop effective viscosity models, including depletion layer effects. For the narrower channels, the depleted volume fraction is no longer negligible and we need to develop models for larger depletion layers up to $\delta/h \sim 0.1$. First, we develop the effective viscosity models, before we develop a depletion layer thickness model based on the Ma and Graham dumbbell model, representing a coarse grained polymer.

5.1. Effective viscosity model with depletion

The effective viscosity is a function of Weissenberg number Wi, channel width h, depletion layer thickness δ, polymer chain length N, and polymer

concentration c,

$$\mu_e = \mu_e(Wi, h, \delta, N, c). \tag{13}$$

Salinity (electrolyte contents) and/or polymer solubility will also play a role through their effects on the polymer extension. The depletion layer thickness is a function of the channel width h, but also of the variables Wi, N, c,

$$\delta = \delta(h, Wi, N, c). \tag{14}$$

The effective viscosity is reduced by the depletion layer, and one can define a correction factor f_d,

$$\mu_e(Wi, h, \delta, N, c) = \frac{\mu_e^0(Wi, N, c)}{f_d(\delta/h)} \tag{15}$$

where μ_e^0 is the effective viscosity for a homogeneous polymer solution throughout the flow volume (no depletion layer), and f_d is an increasing function of the depleted volume fraction δ/h [48, 10]. In the following, we develop algebraic models for the correction factor f_d, accounting for depletion layers that span a significant fraction of the channel volume.

5.1.1. Newtonian flow

Here we assume Newtonian flow with a step-wise viscosity profile, with water viscosity in the near-wall depletion layer and a constant higher viscosity in the core volume of the channel. The Newtonian approximation is valid for polymer solutions if Wi is near and below unity (Appendix C). For thin depletion layers where $\delta/h \ll 1$, it has been shown earlier that the effective viscosity is approximately [10, 49]

$$\mu_e = \frac{\mu_e^0}{1 + 6(\mu_b/\mu_w - 1)(\delta/h)}, \tag{16}$$

where μ_b is the viscosity in the core flow and μ_w is the pure water viscosity in the depleted layer. For narrow depletion layers, the concentration of polymer is not elevated much in the core, and we can take the core viscosity equal to the viscosity of the homogeneous polymer solution, $\mu_b = \mu_e^0$. The same form holds for thin layer approximations in pipe flow [48, 50], but with the numerical factor 6 replaced by 4.

If the depletion layer is a significant fraction of the channel width, we obtain the Newtonian approximation (Appendix D)

$$\mu_e = \frac{\mu_e^0}{\frac{\mu_e^0}{\mu_b}(1-2\delta/h)^3 + 6\frac{\mu_e^0}{\mu_w}\frac{\delta}{h}(1-\delta/h)}, \tag{17}$$

where the core viscosity is elevated due to increased concentration in the core volume. We assume a step-wise concentration profile (being zero in the depletion layer), and we use the linear form (Appendix D)

$$\mu_b = \mu_w(1 + \alpha\frac{C_0}{1-\frac{2\delta}{h}}), \tag{18}$$

where the viscosity increases in proportion to the polymer concentration, appropriate for a dilute solution. Here C_0 is the concentration of polymer for the homogeneous solution without depletion layers, and α is a constant. For thin depletion layers $\delta/h \ll 1$, $\mu_b \to \mu_e^0$, and we recover the thin-layer model (16).

5.1.2. Power law flow

For higher Weissenberg number, we may expect shear thinning effects in the core flow, even though the shear rates are diminishing towards the midpoint of the channel. Algebraic forms are possible if we assume power

law behavior in the core. The depletion layer is still Newtonian with a lower water viscosity. For power law fluids, the shear viscosity is

$$\mu = \mu_{00}|\dot{\gamma}|^{(n-1)}, \tag{19}$$

where μ_{00} depends on polymer concentration, and the index $n < 1$ for shear thinning. The effective viscosity for an *un-depleted* power law fluid with constant μ_{00} (homogeneous polymer distribution) is

$$\mu_e^0 = \frac{kG}{U} = \frac{k}{B}G^{1-1/n} \tag{20}$$

where B is a constant (Appendix C) and $k = a^2/3$ is the permeability coefficient for the channel with $a = h/2$. The cross sectionally averaged viscosity in the channel is

$$\langle\mu\rangle = k_{eff}\frac{G}{U} = \mu_{00}\langle\dot{\gamma}\rangle^{n-1} = \mu_{00}(Wi/\lambda)^{n-1}, \tag{21}$$

in terms of a modified permeability k_{eff} (Appendix C). Thus, the effective viscosity for the homogeneous polymer solution is also a power law, since

$$\mu_e^0 = (k/k_{eff})\langle\mu\rangle = (k/k_{eff})(\mu_{00}/\lambda^{n-1})(Wi)^{n-1} \equiv \mu_e^{00}(Wi)^{n-1}. \tag{22}$$

For depletion layers that are not restricted to be thin, we obtain the approximation (Appendix D)

$$\mu_e = \frac{\mu_e^0}{\left(\frac{\mu_{00}}{\mu_0}\right)^m(1-2\delta/h)^{m+2} + a^*(\tau_w)\frac{\delta}{h}(1-\delta/h)}, \tag{23}$$

where a^* is a decreasing function of the wall shear stress $\tau_w = Gh/2$ reducing the correction for higher shear rates,

$$a^*(\tau_w) = \frac{2\mu_{00}^m(m+2)}{\mu_w\tau_w^{m-1}}, \tag{24}$$

and $m = 1/n$. Increased polymer concentration in the core is accounted for by adjusting the viscosity coefficient μ_0 according to (Appendix D),

$$\mu_0 = \mu_w(1 + \beta \frac{C_0}{1 - \frac{2\delta}{h}}), \tag{25}$$

and for vanishing depletion layer, $\mu_0 \to \mu_{00}$ by definition.

For Newtonian flow, $m = 1$, $\mu_0 = \mu_b$, $\mu_{00} = \mu_e^0$ and $a^* = 2(m+2)\mu_b/\mu_w = 6\mu_b/\mu_w$, and (23) reduces to the thick-layer Newtonian form (17). For thin depletion layers, $\delta/h \ll 1$, (23) reduces to the power law model

$$\mu_e = \frac{\mu_e^0}{1 + [a^*(\tau_w) - 2(m+2)](\delta/h)}, \tag{26}$$

and the thin-layer Newtonian form (16) is recovered with $m = 1$, and $a^* = 6\mu_b/\mu_w$. Thus, all four representations (16,17,26,23) are consistent with each other.

5.2. Comparison to simulation data

The essential quantity that controls the viscosity reduction in both the Newtonian and shear thinning cases is the *relative* depletion width δ/h (the volume fraction of the depleted layer). We will test all four descriptions below, and to this end, we take the measured depletion layer thickness as input to the effective viscosity model.

The different models are compared to the data for the $N = 60$ chain in figure 5 where the concentration increase in the core is ignored (setting $\mu_b = \mu_e^0$ for the Newtonian model, and $\mu_0 = \mu_{00}$ for the power law model), and in figure 6 where the concentration increase is accounted for. For the Newtonian model, we calibrated μ_e^0 to the measured viscosity at $Wi = 1.5$ for the largest channel width (150 nm), assuming a negligible effect from

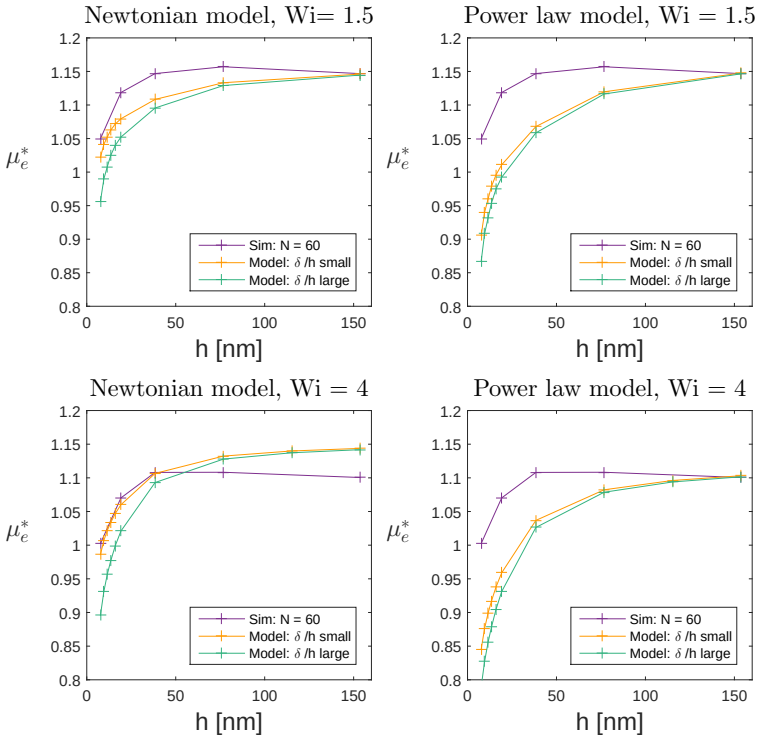

Figure 5: Effective viscosity as function of channel height, and ignoring the concentration increase in the core. Left: Newtonian model. Right: Power law model.

depletion at this width (upper left panel). The same value was used for $Wi = 4$ (lower left panel). The measured viscosity for $Wi = 4$ is lower than for $Wi = 1.5$, due to shear thinning.

The Newtonian model (upper left) provides a reasonable fit to the data, including the effect of reduced viscosity with narrower channels. It is however evident that the difference between the thin depletion layer approximation (orange) and the more general model approximation (green) is only marginal, with the thin layer approximation giving slightly larger viscosity values. The

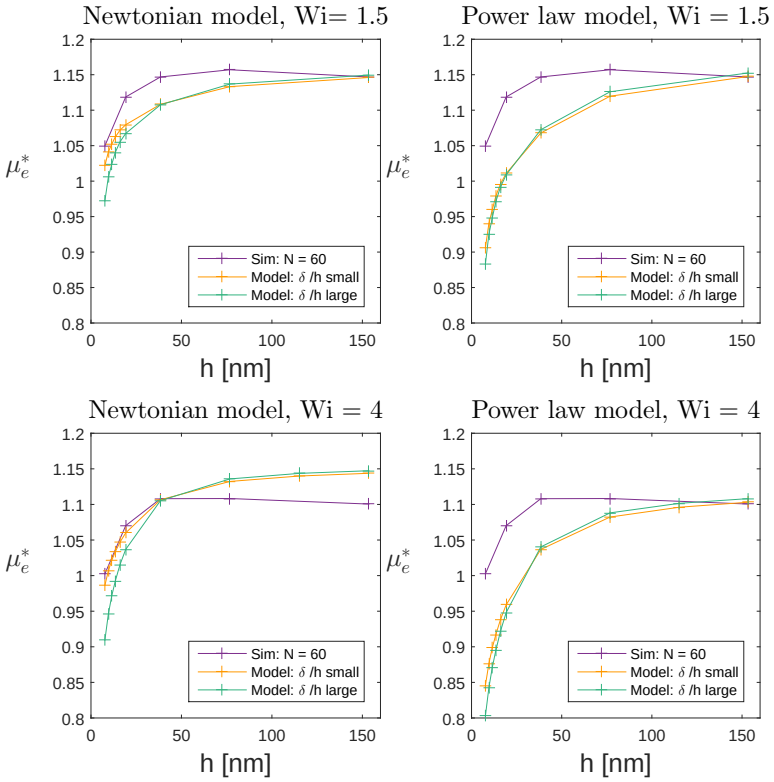

Figure 6: Effective viscosity as function of channel height and accounting for the concentration increase in the core for the thick depletion layer model (green). Left: Newtonian model. Right: Power law model.

Newtonian model overestimates the effective viscosity for the higher Weissenberg number (lower left), due to the shear thinning effect in the measured viscosity values. The models are not valid for values of δ/h above about 0.2 where the model assumptions break down, even for the more general one. Effective viscosity values below 1.0 are therefore an indication where the models break down.

For the power law model, $\mu_e^0 = \mu_e^{00}(Wi)^{n-1}$. The index n was estimated

by taking the ratio R of the measured viscosities at (150 nm) at $Wi = 1.5$ and $Wi = 4.0$ with $R = (1.5/4.0)^{n-1}$, again assuming negligible depletion layer effect at this width. We found $n \simeq 0.9$, and μ_0 could then be determined from either of the measured viscosity values. Furthermore, we could set $\mu_{00} = \mu_0$ at this width.

The power law models have a more gradual increase of the effective viscosity than the simulation data show, and does not offer a better fit to the data than the Newtonian model. The reason for the more gradual increase is an overall lower sensitivity to the variation in δ/h. The average shear in the core flow is lower than the average shear corresponding to the average Weissenberg number. It is therefore likely that the shear thinning effect in the core flow is not that important. Furthermore, for very low shear rates near the midpoint of the channel, the power law grossly overestimates the viscosity where it should reach the upper Newtionian Carreau-value. We therefore conclude that the Newtonian model offers a robust alternative to the power law model, even though the Newtonian model does not account for the intrinsic shear thinning in the fluid.

A "hybrid" alternative model would be to use the Newtonian form of the correction factor (denominator in the models) to obtain a good fit to the variation with channel width, with a power law or Carreau model for the uncorrected effective viscosity μ_e^0.

For significant depletion layer thickness relative to the channel width, the concentration increase in the core flow increases the core viscosity value. Figure 6 shows the resulting viscosity profiles (green), when we assume a linear increase of viscosity with the concentration, according to the formu-

lation above. The thin layer approximations do not incorporate this effect by definition. The Newtonian model (17) responds with lowered μ_e^0/μ_b in the denominator, increasing the effective viscosity. Similarly, the power law model responds via lowered μ_{00}/μ_0 in the denominator, again increasing the effective viscosity. However, this concentration effect is only marginal for dilute solutions.

6. Depletion layer model

A model for the depletion layer thickness $\delta(h, Wi, N, c)$ is needed as input to the effective viscosity model to obtain a complete effective viscosity model. We developed a depletion layer thickness model based on the migration model of Ma and Graham [15] for dumbbells. The dumbbell model allows for a rigorous calculation of drift fluxes due to viscous hydrodynamic interaction with the wall and gradient diffusion, and serves as a "minimal" physical model for the concentration profile over the channel cross section. The dumbbell represents the highest level of coarse graining of the polymer molecule, and the model parameters must be interpreted as coarse graining parameters when representing long polymer chains.

6.1. Ma and Graham channel flow model

The cross-channel mass flux of non-interacting dumbbells perpendicular to a flat wall is, to leading order,

$$j = V_d(y)n - D\partial_y n, \tag{27}$$

where V_d is the local drift velocity due to viscous hydrodynamic interaction between the dumbbell and the solid wall, n is the number density, and D is

the diffusivity due to Brownian motion,

$$D = \frac{kT}{12\pi\eta a}, \tag{28}$$

where a is the effective hydrodynamic radius of the dumbbell, and η is the solvent viscosity.

In Poseuille channel flow between two flat walls separated by a distance h, one can superpose the two single wall interactions as an approximation for the net drift velocity,

$$V_d(y) = \frac{K(y)}{y^2} - \frac{K(h-y)}{(h-y)^2}, \tag{29}$$

where the variation with $1/y^2$ is due to viscous interaction with the wall. The drift velocity is necessarily an antisymmetric function around the midpoint of the channel, directed away from both walls and into the core of the channel, and $K(y) = K(h-y)$ is symmetric,

$$K(y) = \frac{3}{64\pi\eta n}(N_1(y) - N_2(y)), \tag{30}$$

in terms of the normal stress difference $N_1 - N_2$ of the dumbbells. For the finite extensible FENE-P dumbbell one obtains [51],

$$\frac{N_1 - N_2}{nkT} = \frac{\tau_{xx}^p}{nkT} = 18S^2. \tag{31}$$

where for all Weissenberg numbers [52],

$$S(y) = \frac{1}{3}\sqrt{\frac{2(3+b)}{3}} sinh\left[\frac{1}{3} asinh\left(\frac{\hat{Wi}(y)\, b}{108}\left(\frac{54}{3+b}\right)^{3/2}\right)\right], \tag{32}$$

where $\hat{Wi}(y) = \lambda\dot{\gamma}(y)$ is the local Weissenberg number. In plane parallel flow, $N_1 = \tau_{xx}^p$ in terms of the polymer normal stress in the flow direction, and $N_2 = 0$.

6.2. Coarse graining interpretation

The dumbbell extension parameter b is the ratio between potential and thermal energy,

$$b = HR_0^2/kT, \tag{33}$$

in terms of the FENE-P Hooke spring force parameter H, and the the maximum spring extension R_0. In our context of coarse grained polymer chains, we may adopt an average value for the potential energy between two coarse grained DPD units. We expect this to be on the order of unity based on the principle of equipartition; the average potential energy in the Hookean potential between the DPD beads must be comparable to kT, since the spring force interaction between two beads represents one degree of freedom. We obtained reasonable correspondence to the simulation data with $b = 1.5$.

The local depletion length scale is

$$L_d(y) = \frac{K(y)}{D} = \frac{9}{16}\frac{N_1 - N_2}{nkT}a = \frac{162}{16}S^2(\hat{W}i(y), b)a. \tag{34}$$

In the original dumbbell model, a is the effective hydrodynamic radius of the dumbbell, where crossflow diffusion is reduced with increasing a. In our case, we interpret this parameter as a correlation length or persistence length over which the polymer chain remains approximately as a linear unit that can be represented by the dumbbell or a pair of beads in the DPD model. The polymer chain resembles that of a biased random walk due to thermal fluctuation and shear forces, and the random walk step length corresponds to the correlation length along the chain. We expect that the persistence length varies with the strain rate or Weissenberg number. The parameter b can be interpreted as the potential/thermal energy ratio over one persistence length.

6.3. Depletion layer model

In steady state there is no net mass flux of polymer normal to the wall ($j = 0$), and the solution to (27) for the polymer number density profile across the channel is

$$n(y) = n(h/2)exp\left[\int_{L/2}^{y} L_d(z)\left(\frac{1}{z^2} - \frac{1}{(h-z)^2}\right)dz\right]. \tag{35}$$

It is convenient to define the depletion layer thickness where the concentration profile is lowered to a certain value. We used the half-value in the data analysis, in which case

$$\int_{h/2}^{h-\delta^*} L_d(z)\left(\frac{1}{z^2} - \frac{1}{(h-z)^2}\right)dz = \ln(1/2) \simeq -0.7, \tag{36}$$

where δ^* is the depth of the depletion layer predicted by the model, and the local depletion length is defined by (34). The integral is evaluated numerically (trapez integration) up to δ^* where the equation balances. As a first order approximation that does not require detailed knowledge of the velocity profile, we take the local Weissenberg number to vary linearly through the channel (as in Newtonian flow),

$$\hat{Wi}(z) = 2Wi(\frac{2}{h}z - 1), \tag{37}$$

where Wi is the average Weissenberg number. This is now used in (34). Thus, the depletion layer model can be formulated as

$$\delta^* = \delta^*(h, Wi, a, b). \tag{38}$$

Asymptotes to (36) are derived in Appendix E. For high $Wi \gg 1$ we obtain to first order in δ^*/h the simple explicit formula

$$\delta^* = \frac{\overline{L}_d}{1 + 4\overline{L}_d/h}. \tag{39}$$

with a characteristic depletion length scale $\overline{L}_d$ that represents the typical value across the entire depletion layer. By using the asymptotic form of S [53], we find

$$\overline{L}_d = \frac{9}{16\ln(2)} 2^{1/3} a (bWi)^{2/3}. \tag{40}$$

This high Weissenberg number approximation worked well also for $Wi = 4$, as we shall see. For very small $Wi \ll 1$ we obtain a similar useful form to first order

$$\delta^* = \frac{\overline{L}_d}{1 + 4q\overline{L}_d/h}, \tag{41}$$

and with the lower asymptotic form of S [53],

$$\overline{L}_d = \frac{18}{16\ln(2)} \left(\frac{b}{b+3}\right)^2 4aWi^2 \tag{42}$$

$$q = 5/2 - \ln(4) \simeq 1.11. \tag{43}$$

This approximation is valid only for near Newtonian flow where $Wi \ll 1$ everywhere in the channel.

6.4. Comparison to simulation data

The asymptotic value of $\delta^*(h, Wi)$ for large h is controlled by the polymer correlation length a. A good fit to the simulation data was obtained with $a = 5$ for $Wi = 1.5$, and $a = 1.8$ for $Wi = 4$, and the a parameter is expected to vary with Wi as discussed above. The energy ratio b was fixed at 1.5 for all cases.

The integral model (36) for δ^* gives a fair representation of our simulation data for δ (Figures 7 and 8 for the N = 60 polymer chain). This simplified dumbbell model description provides a qualitatively correct variation of the depletion layer thickness with channel width, consistent with the behavior

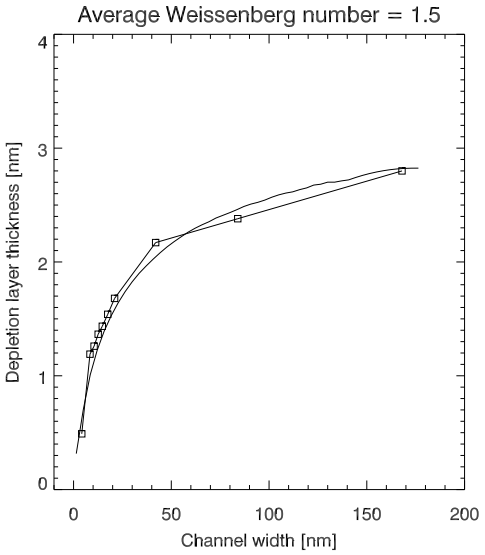

Figure 7: Depletion layer thickness model (full line) as function of channel height for $Wi = 1.5$ plotted together with the simulation results (squares) for the N = 60 polymer chain.

reported elsewhere in the literature (see the introduction). Thus one can explain the simulation data in terms of hydrodynamic drift away from the wall, and gradient diffusion back towards the wall.

For large channel width, only viscous interaction with the nearby wall is effective, and $\delta^* \to \overline{L}_d(Wi)$ which increases with Wi. That this limiting value increases with Weissenberg number is also seen by comparing Figures 7 and 8. Confinement effects due to interaction from both walls become significant when $h \to \overline{L}_d$, and the depletion layer is reduced to values below the single wall prediction $\overline{L}_d$. In the regime $h \ll \overline{L}_d$ (small channel width or high Weissenberg number), $\delta^* \simeq h/4$ with this model. However, the two depletion layers span most of the channel in this case and the accuracy is

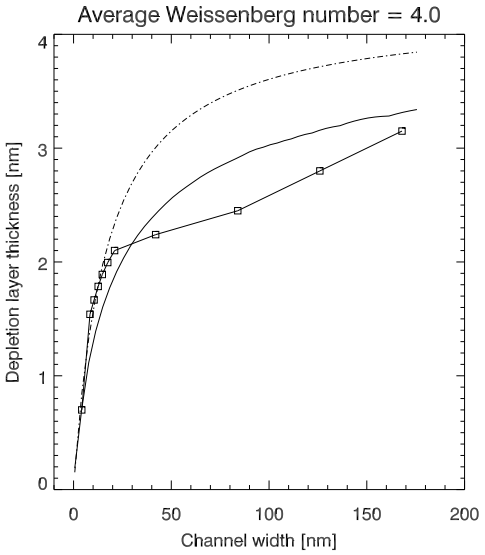

Figure 8: Depletion layer thickness model (full line) as function of channel height for $Wi = 4.0$ plotted together with the simulation results for the N = 60 polymer chain. The dotted line is the high Weissenberg number approximation.

then dependent on the validity of linear superposition of the drift velocities generated by the two walls, which is assumed in the Ma and Graham model.

Increased diffusivity and back diffusion towards the walls corresponds to lowered $\overline{L}_d$ in general, and smaller depletion layer thickness, regardless of channel width. Increased shear or Weissenberg number increases the depletion layer thickness through the viscous wall interaction. For high Weissenberg number, the model predicts $\delta^* \simeq h/4$ as above. The high Weissenberg number limit (39) is plotted in figure 8 (dotted line) together with the simulation results and the general model (36). This form gives a significant overprediction, although the variation with channel width is qualitatively correct.

For very small Weissenberg number $\delta^* \simeq \overline{L}_d$ by (41) and the model predicts $\delta^* \to 0$ for vanishing shear. However, in this limit, direct steric interaction with the wall becomes important and one may need a generalized model of the type

$$\delta^* = \frac{\overline{L}_d}{1 + 4q\overline{L}_d/h} + \delta_{\text{Steric}}, \tag{44}$$

and models for sterically generated depletion layers without flow, δ_{Steric}, can be found in the literature [13].

7. Discussion

Cuenca and Bodiguel [10] used HPAM200K ($2{\times}10^5$ g/mol) and HPAM8M (8×10^6 g/mol) solutions and measured the effective viscosity in microchannels. The shorter polymer chains had Newtonian behavior, while the longer chains (8M) had shear thinning behavior. These authors concluded that the slip length $b = (\mu_b/\mu_w)\delta$ decreased with confinement, in agreement with our results. By imposing a constant wall shear stress the estimated slip length showed a stronger increase with channel width for the 8M polymer. This is consistent with our model if longer chains correspond to larger coarse grained segment length a, which gives a higher asymptotic δ for wider channels.

Our simulations showed a significant reduction of viscosity only for channel widths below about 50 nm, whereas Cuenca and Bodiguel [10] found significant reductions also for larger channel widths in the micron to submicron range. The most likely reason for this that HPAM polymers are longer relative to the DPD model we used. Since there is consistency between DPD and hydrodynamics [12], qualitatively correct hydrodynamic behavior is then expected in terms of effective viscosity and polymer migration for

the given polymer model. Hence, the simulations generated a valid dataset over which the viscosity models and depletion layer model could be developed. Applications to real HPAM polymers is then possible by re-tuning the model parameters a and b, and using the effective viscosity models as they are formulated.

The literature establishes that steric repulsion (direct wall interaction) at the wall seems to be an important depletion mechanism for low or vanishing Wi. As the shear rate increases, the polymer size in the wall normal direction decreases and δ can be smaller with increasing shear rates. We did not observe this effect possibly due to the fact that we did not implement sufficiently small Wi. For very narrow channels, the hydrodynamic migration (derived from Stokesian dynamics) cancels to a large degree [15, 8], and the near wall steric repulsion may be more important for a wider range in Wi.

The diffusive flux smooths out the concentration gradients in general, but the diffusivity is anistotropic and depends on the degree of polymer stretching via the Weissenberg number. The model we derived does not incorporate this anisotropy. In the simulations, we observed a tendency to "freeze in" the polymer chains in the solvent as they stretched out, due to lowered diffusivity perpendicular to the flow direction. Ensemble averaging over several simulation runs had to be conducted in some cases, to obtain good statistics of the concentration profiles and less dependency of the initial condition (the positioning of the polymer in the domain initially).

A characteristic feature at high enough Wi in Poiseuille flow, is the emergence of two concentration peaks around the channel centerline [8]. As the polymer chains tend to stretch out, they concentrate at an intermediate posi-

tion between the wall and the centerline. Some authors [19] have attributed this to hydrodynamic Segre-Silberberg forces generated by the shear gradients, and the wall-polymer hydrodynamic interaction. Higher order corrections to the effective viscosity are expected as a consequence of these concentration variations throughout the channel. The viscous shear stress is in general a linear function over the cross section,

$$\tau_{xy} = \mu(C, y)\partial_y u_x = |\partial_x p| y \tag{45}$$

$y \in [-h/2, h/2]$, where the viscosity increases with polymer concentration C. Locally low/high viscosity corresponds to high/low velocity gradient, for a given stress value, and the velocity profile changes. These effects were not accounted for the effective viscosity models, as we assumed a step-wise concentration profile. If such effects were to the included, we would not be able to construct a simple algebraic model.

For porous media we expect additional effects in the apparent viscosity from a more complex geometry. Extensional "thickening" is an important visco-elastic effect that can occur in the bottle-neck geometry of pore throats where polymer stretching in the flow direction and subsequent compression/relaxation of the polymer chains constitutes extra dissipation and flow resistance [54]. However, Berea sandstone cores with HPAM solutions show an increased effective viscosity only at estimated shear rates of about 100 s^{-1} and higher [3]. Thus, we expect that extensional thickening can happen near well bores, but not often further into the reservoir.

8. Conclusion

Algebraic effective viscosity models and a depletion layer model were developed based on simulations and existing hydrodynamic theory. Application of the models to real polymers is possible by retuning the depletion layer coarse graining parameters a (persistence length) and b (energy ratio over the persistence length). The effective viscosity models can be used as formulated. For low Weissenberg number, we recommend using the Newtonian version of the effective viscosity model. For higher average Weissenberg number, we recommend using the Newtonian form of the correction factor f_d, if the Weissenberg number in the core volume is less than unity.

The effective viscosity is lowered for narrower channels because the depleted *volume fraction* δ/h increases. Experimental evidence show that this reduction is significant for narrower channels in the micron to sub-micron range [10], characteristic of porous reservoir media (sandstone or chalk).

The depletion layer thickness δ is reduced with smaller channel width h, even though the volume fraction δ/h increases. The main reason for the reduction of δ with smaller h is that the hydrodynamic forces that drive migration away from the walls tend to cancel[15]. The simulation results confirmed this behavior. With the development of depletion layers, the increased concentration in the core regions of the channel leads to increased gradient diffusion flux back towards the walls. This limits the growth of the depletion layer thickness with increasing Wi, for moderate h. When the wall separation h is sufficiently large, such that the confinement effect vanishes, the depletion layer thickness is completely determined by the Weissenberg number (shear rate). For very low Weissenberg numbers (lower than we

used), the migration vanishes and the polymers are closer to the wall. Steric interactions may then be important such that the depletion layer thickness can be reduced with higher shear rates due to polymer stretching.

Acknowledgments T. L. Palmer was funded by the IOR center via the Research Council of Norway (RCN), ConocoPhillips Skandinavia AS, DONG Energy AS Denmark, Eni Norge AS, ENGIE, Lundin Norway AS, Maersk Oil Norway AS, Statoil Petroleum AS, Wintershall Norge, Schlumberger Norge AS, and Halliburton. T. L. Palmer thanks Aksel Hiorth and the University of Stavanger for hosting her project, and Institute for Energy Technology (IFE) for computational facilities. A. Stavland, E. Jettestuen, J. L. Vinningland, and A. Hiorth provided support and comments to our work. G. Baardsen was funded by IFE for developing the parallel version of the code. G. Baardsen thanks Ø. Jensen and E. Sollum for helpful discussions. R. Skartlien was funded by the IOR center and IFE. The prototype code was developed by R. Skartlien in the earlier CRI FACE, partially supported by RCN. We used the freewares VISIT, TeXstudio and makebst.

Appendix A. Achieving high Schmidt numbers

The Schmidt number is the ratio between the diffusivity D of a particle (Brownian diffusion) and the kinematic viscosity ν; $Sc = \nu/D$. It is relatively straightforward in DPD to increase Sc to several hundred (it is of the order of 1000 in common fluids) by adjusting the dissipative and stochastic force models through the standard DPD weights [18]

$$w_D = w_R^2 = (1 - r/R_d)^q, \tag{A.1}$$

by lowering the power law exponent q below the standard value of 2, and increasing the dissipative/stochastic force cutoff radius R_d, with $R_d > R_c$. Increasing γ increases the Schmidt number further. We chose the values $q = 1/2$, $R_d = 1.2$ and $\gamma = 27$. This gives a Schmidt number of $Sc = 600$ [18], without a prohibitive increase of computational time (about a factor 4 longer). $Sc > 500$ gives reasonable agreement with measured polymer concentration profiles [17].

Appendix B. Processing of intra-bead polymer forces

In the domain-decomposition algorithms of Plimpton [39], the data of particles residing within one interaction cutoff length from a processor domain P is copied to calculate forces between beads in domain P and beads in neighboring processor domains. In a similar way, to evaluate bond forces across processor domains, we have copied data of all bonded beads located within one bond-force cutoff length, R_B, from the processor domain in which the bond force is evaluated. For example, to calculate bond forces in processor domain P, we copy data from neighboring processor domains $Q, R, S, \ldots$ to domain P, so that data of all bonded beads that are within the distance R_B from the domain P is included. We have required that all sides of the processor domains are larger than the bond-force cutoff.

Polymer degradation/breakup can be modelled by using a lower value of the spring constant C. In that case, it is convenient to evolve the polymer dynamics separately with smaller time steps for better prediction of the number of broken bonds. Such sub-cycling of the polymers is an option that we have implemented, but we did not use it for the current work. To enable use of dif-

ferent time step lengths for interbead and bond forces, respectively, we have implemented a parallelized version of the rRESPA algorithm of Plimpton *et al.* [41].

Appendix C. Shear thinning and power law rheologies

The Carreau model governs a smooth shear thinning transition between the zero shear viscosity μ_b and the lower, solvent viscosity μ_∞ at high shear rate,

$$\mu = \mu_\infty + \frac{(\mu_b - \mu_\infty)}{[1 + (\lambda\dot{\gamma})^x]^{\frac{1-n}{x}}} = \mu_\infty + \frac{(\mu_b - \mu_\infty)}{[1 + (\hat{Wi})^x]^{\frac{1-n}{x}}}, \tag{C.1}$$

where the local shear rate is $\dot{\gamma}$. Here, $1 - n > 0$, and the fit $x = 2$ is usually made. In the shear thinning regime $\hat{Wi} \gg 1$, a power law behavior is recovered for

$$\mu - \mu_\infty = \frac{(\mu_b - \mu_\infty)}{(\hat{Wi})^{1-n}}. \tag{C.2}$$

The exponent n varies with concentration and molecular mass [3],

$$n = n_0 + bX, \tag{C.3}$$

and $1-n$ is in the range 0.1 to 0.6 for $X = [\mu_0]c$ in the range 0 to 20 (in terms of the intrinsic viscosity $[\mu_0]$ and the concentration by mass, c, of polymer), and the relaxation time λ is in the range 0 to 4 s. For strict power law fluids,

$$\mu = \mu_0|\dot{\gamma}|^{(n-1)}, \tag{C.4}$$

and the average velocity in a channel without slip is

$$U = B(h, m, \mu_0)G^m = \frac{(h/2)^{m+1}}{m+2}\left(\frac{G}{\mu_0}\right)^m = \frac{(h/2)^{m+1}}{m+2}\left(\frac{2\tau_w}{h\mu_0}\right)^m, \tag{C.5}$$

where B is a constant, and the effective viscosity becomes

$$\mu_e^0 = \frac{kG}{U} = \frac{k}{B} G^{1-1/n}. \tag{C.6}$$

The average power law viscosity over the channel volume is

$$\langle \mu \rangle = k_{eff} \frac{G}{U} = \mu_0 \langle \dot{\gamma} \rangle^{n-1}, \tag{C.7}$$

with an effective permeability

$$k_{eff} = \frac{a^2}{(2+1/n)(1+1/n)^{n-1}}. \tag{C.8}$$

and the average shear rate over the channel is

$$\langle \dot{\gamma} \rangle = \frac{1}{a} \int_{-a}^{0} \partial_y u(y) dy = \frac{u(0)}{a} = \frac{(G/\mu_0)^m}{m+1} a^m. \tag{C.9}$$

Appendix D. Effective viscosity with depletion layers

With relatively thin depleted layers of thickness $\delta/h \ll 1$ near both walls, the velocity profile will appear shifted to higher values. The shape of the profile will also be affected, but this can be considered as a higher order effect. One can define a slip velocity V_s at the transition between the depleted layer and the bulk velocity profile (the fluid velocity at the wall is always zero).

For depletion layers that are not thin, with δ/h in the range 0.1-0.2 for very narrow channels below 50 nm, the flow rate in the depletion layer is significant, and it has to be added to the flux of the core flow. Furthermore, the boundary shear stress in the transition between the core flow and the depletion layer is smaller than the wall shear stress.

We now assume that the velocity profile is linear in the depletion layers, and that the boundary conditions for the core flow velocity profile is the slip

velocity and the shear stress at the core flow boundary. The average velocity over the channel is now

$$U = \frac{1}{h}\left[V_s\delta + (U^* + V_s)h^*\right] \tag{D.1}$$

where $U^* + V_s$ is the average velocity of the core flow, and $h^* = h(1 - 2\delta/h)$ is the width of the core flow. We note that the linear approximation is a first order approximation for the velocity profile in the depletion layer, valid for sufficiently small δ/h.

Appendix D.1. Newtonian fluids

For Newtonian flow in the core,

$$U^* = \frac{h^*\tau^*}{6\mu_b} \tag{D.2}$$

where the boundary shear stress is

$$\tau^* = \tau_w(1 - 2\delta/h). \tag{D.3}$$

This gives a mean velocity of

$$U = V_s(1 - \delta/h) + \frac{h\tau_w}{6\mu_b}(1 - 2\delta/h)^3. \tag{D.4}$$

The effective viscosity with a Newtonian core is then

$$\mu_e = \frac{\mu_e^0}{(1 - \delta/h)V_s/U^0 + \frac{\mu_e^0}{\mu_b}(1 - 2\delta/h)^3}, \tag{D.5}$$

where

$$U^0 = \frac{h\tau_w}{6\mu_e^0} \tag{D.6}$$

is the average velocity without a depletion layer, and the bulk viscosity of the uniform polymer solution is equal to the effective viscosity without depletion,

μ_e^0. With a linear velocity profile in the depletion layer, $V_s = \dot{\gamma}_w \delta = \tau_w \delta / \mu_w$, and

$$V_s/U^0 = 6\frac{\mu_e^0}{\mu_w}\frac{\delta}{h}, \tag{D.7}$$

giving

$$\mu_e = \frac{\mu_e^0}{\frac{\mu_e^0}{\mu_b}(1-2\delta/h)^3 + 6\frac{\mu_e^0}{\mu_w}\frac{\delta}{h}(1-\delta/h)}. \tag{D.8}$$

This reduces to the thin depletion layer approximation in the limit $\delta/h \ll 1$. For vanishing polymer concentration, the viscosity contrast vanishes, and $\mu_b = \mu_e^0 = \mu_w$, and the correction goes to zero. A Taylor expansion of the denominator to first order in δ/h gives

$$(1-2\delta/h)^3 + 6\frac{\delta}{h}(1-\delta/h) \to 1 - 6\delta/h + 6\delta/h \tag{D.9}$$

which is consistent with vanishing correction to the effective viscosity, provided that δ/h is sufficiently small, according to the model definition.

When the depletion layer is thick, we must also correct for the effect of increasing polymer concentration in the core. We take

$$\mu_b = \mu_w(1 + \alpha\frac{C_0}{1-\frac{2\delta}{h}}) \tag{D.10}$$

where the variation with δ accounts for a step function in concentration, being zero in the depletion layer, and α is a constant that can be estimated from the data, and C_0 is the polymer concentration for a uniform distribution of polymer in the channel.

Appendix D.2. Power law fluids

For power law shear thinning in the core,

$$U^* = \frac{h^* {\tau_w^*}^m}{2(m+2)\mu_0^m} \tag{D.11}$$

and μ_0 is a function of polymer concentration. As before, the boundary shear stress is

$$\tau^* = \tau_w(1 - 2\delta/h). \tag{D.12}$$

This gives a mean velocity of

$$U = V_s(1 - \delta/h) + \frac{h\tau_w^m}{2(m+2)\mu_0^m}(1 - 2\delta/h)^{m+2}. \tag{D.13}$$

The effective viscosity with a power law core is then

$$\mu_e = \frac{\mu_e^0}{(1 - \delta/h)V_s/U^0 + \left(\frac{\mu_{00}}{\mu_0}\right)^m (1 - 2\delta/h)^{m+2}}, \tag{D.14}$$

where

$$U^0 = \frac{h\tau_w^m}{2(m+2)\mu_{00}^m} \tag{D.15}$$

is the average velocity without a depletion layer and μ_{00} is the lower value without depletion where the polymers are distributed uniformly throughout the full cross section of the channel, and $\mu_e^0 = \mu_{00}(Wi)^{n-1}$ is effective viscosity without depletion, which is also a power law when the core rheology spans the whole channel. The wall shear stress is $\tau_w = Gh/2$. With a linear velocity profile in the depletion layer, $V_s = \dot{\gamma}_w\delta = \tau_w\delta/\mu_w$, we get

$$\frac{V_s}{U^0} = \frac{2\mu_{00}^m(m+2)}{\mu_w\tau_w^{m-1}}\frac{\delta}{h} \equiv a^*(\tau_w)\frac{\delta}{h}. \tag{D.16}$$

giving

$$\mu_e = \frac{\mu_e^0}{\left(\frac{\mu_{00}}{\mu_0}\right)^m (1 - 2\delta/h)^{m+2} + a^*(\tau_w)\frac{\delta}{h}(1 - \delta/h)}. \tag{D.17}$$

Again, this limits to the thin depletion layer approximation for $\delta/h \ll 1$. In the zero viscosity contrast limit, corresponding to small polymer concentration, $m \to 1$ and $\mu_0 = \mu_{00} = \mu_w$, and we recover the Newtonian form with the same limiting behavior of zero correction to the effective viscosity.

The effect of increasing polymer concentration in the core for increasing depletion layer thickness is reflected in the power law viscosity coefficient,

$$\mu_0 = \mu_w(1 + \beta \frac{C_0}{1 - \frac{2\delta}{h}}) \tag{D.18}$$

where the variation with δ accounts for a step function in concentration, being zero in the depletion layer, and β is a constant that can be estimated from the data, and C_0 is the polymer concentration for a uniform distribution of polymer in the channel. For $\delta = 0$, $\mu_0 = \mu_{00}$.

Appendix E. Depletion layer model limits

Appendix E.1. High Weissenberg number

For large Weissenberg number the normal polymer stresses can be approximated by [53],

$$\frac{N_1 - N_2}{nkT} \simeq 2^{1/3}(b\hat{W}i)^{2/3}. \tag{E.1}$$

In this case, $\hat{W}i^{2/3}(z)$ varies relatively slowly compared to $1/z^2$ so that we may use a characteristic depletion length scale $\overline{L}_d$ that represents the typical value across the entire depletion layer,

$$\overline{L}_d = \frac{9}{16} 2^{1/3} a(bWi)^{2/3} \tag{E.2}$$

in terms of the average Weissenberg number Wi in the channel, and

$$\overline{L}_d \int_{h/2}^{h-\delta^*} \left(\frac{1}{z^2} - \frac{1}{(h-z)^2} \right) dz = \frac{\overline{L}_d}{\delta^*} \left[\frac{4\delta^*}{h} - \frac{\delta^*/h}{1 - \delta^*/h} - 1 \right] = \ln(1/2). \tag{E.3}$$

Then, to first order in δ^*/h,

$$\delta^* = \frac{\overline{L}_d}{1 + 4\overline{L}_d/h}. \tag{E.4}$$

where we now incorporate the factor $\ln(1/2)$ in $\overline{L}_d$.

Appendix E.2. Low Weissenberg number

For small Weissenberg number, one obtains the asymptote [53]

$$\frac{N_1 - N_2}{nkT} \simeq 2\left(\frac{b}{b+3}\right)^2 \hat{Wi}^2. \tag{E.5}$$

The characteristic depletion length can then be written

$$L_d(z) = \frac{18}{16}\left(\frac{b}{b+3}\right)^2 \hat{Wi}^2 a. \tag{E.6}$$

We take the Weissenberg number to vary linearly through the channel, as an approximation,

$$\hat{Wi}(z) = 2Wi(\frac{2}{h}z - 1), \tag{E.7}$$

so that the characteristic depletion length is

$$L_d(z) = \frac{18}{16}\left(\frac{b}{b+3}\right)^2 4aWi^2(\frac{2}{h}z-1)^2 \equiv \overline{L}_d(\frac{2}{h}z-1)^2 \tag{E.8}$$

where $\overline{L}_d = A(a,b)Wi^2$. We put E.8 into (36) and integrate, obtaining

$$\overline{L}_d\left[\frac{4}{h}\ln\left(4\frac{\delta^*}{h}(1-\frac{\delta^*}{h})\right) + \frac{1}{h-\delta^*} + \frac{1}{\delta^*} - \frac{4}{h}\right] = \ln(1/2), \tag{E.9}$$

and the factor $\ln(1/2)$ is adsorbed in $\overline{L}_d$ hereafter. By expanding the logarithmic term for the range $0 < \delta^*/h < 1/2$,

$$\ln\left(\frac{\delta^*}{h}\right) + \ln\left(1-\frac{\delta^*}{h}\right) \simeq \left(\frac{\delta^*}{h}\right) - \left(\frac{\delta^*}{h}\right)^2 - \frac{3}{2}, \tag{E.10}$$

one obtains to second order

$$0 = a(\delta^*)^2 + b\delta^* + \overline{L}_d \tag{E.11}$$

$$a = \frac{1}{h} + 4(q+1)\overline{L}_d/h^2 \tag{E.12}$$

$$b = \frac{4\overline{L}_d(p-1)}{h} - 1 \tag{E.13}$$

$$p = \ln 4 - 3/2 \simeq -0.11 \tag{E.14}$$

$$q = 1 - p \simeq 1.11. \tag{E.15}$$

To first order (setting $a = 0$),

$$\delta^* = \frac{\overline{L}_d}{1 + 4(1-p)\overline{L}_d/h}. \tag{E.16}$$

If we omit the log-term that arises from the linear variation of L_d (set $p = 0$ and $q = 1$), we recover the high Weissenberg number form.

References

[1] White, C. M., Mungal, M. G. (2008). Ann. Rev. Fluid Mech., 40:235–256.

[2] Delshad, M., Kim, D. H., Magbagbeola, O. A., Huh, C., Pope, G. A., Tarahhom, F. (2008). Society of Petroleum Engineers, 113620:1–15. doi:doi:10.2118/113620-MS.

[3] Stavland, A., Jonsbråten, H. C., Lohne, A., Moen, A., Giske, N. H. (2010). Society of Petroleum Engineers, 131103:1–15.

[4] Hatzignatiou, D. G., Norris, U. L., Stavland, A. (2013). Journal of Petroleum Science and Engineering, 108:137 – 150. ISSN 0920-4105. doi:http://dx.doi.org/10.1016/j.petrol.2013.01.001.

[5] Beaumont, J., Bodiguel, H., Colin, A. (2013). Soft Matter, 9:10174–10185. doi:10.1039/C3SM51480C.

[6] Jendrejack, R. M., Schwartz, D. C., de Pablo, J. J., Graham, M. D. (2004). The Journal of Chemical Physics, 120(5):2513–2529. doi: http://dx.doi.org/10.1063/1.1637331.

[7] Fang, L., Hu, H., Larson, R. G. (2005). Journal of Rheology, 49(1):127–138. doi:http://dx.doi.org/10.1122/1.1822930.

[8] Graham, M. D. (2011). Annual Review of Fluid Mechanics, 43(1):273–298. doi:10.1146/annurev-fluid-121108-145523.

[9] Aragwal, U. S., Dutta, A., Mashelkar, R. A. (1994). Chemical Engineering Science, 49(11):1693–1717. ISSN 0009-2509. doi:10.1016/0009-2509(94)80057-X.

[10] Cuenca, A., Bodiguel, H. (2013). Phys. Rev. Lett., 110:1083041–5. doi:10.1103/PhysRevLett.110.108304.

[11] Sheng, J. J. (2011). Modern Chemical Enhanced Oil Recovery. Gulf Professional Publishing, Burlington, MA, USA, 1 edition.

[12] Groot, R. D., Warren, P. B. (1997). J. Chem. Phys., 107:4423–4435.

[13] Eisenriegler, E., Maassen, R. (2002). J. Chem. Phys., 116(1):449–450. doi:http://dx.doi.org/10.1063/1.1423323.

[14] Huang, A., Hsu, H.-P., Bhattacharya, A., Binder, K. (2015). J. Chem. Phys., 143(24):2431021–14. doi:http://dx.doi.org/10.1063/1.4929600.

[15] Ma, H., Graham, M. D. (2005). Physics of Fluids, 17(8):0831031–13. doi:http://dx.doi.org/10.1063/1.2011367.

[16] Fan, X., Phan-Thien, N., Yong, N. T., Wu, X., Xu, D. (2003). Phys. Fluids, 15:11–21.

[17] Symeonidis, V., Karniadakis, G. E., Caswell, B. J. Chem. Phys., 125(18):1849021–12.

[18] Fan, X., Phan-Thien, N., Chen, S., Wu, X., Ng, T. Y. Physics of Fluids, 18(6):063102 1–10.

[19] Fedosov, D. A., Karniadakis, G. E., Caswell, B. (2008). The Journal of chemical physics, 128(14):144903 1–14.

[20] Millan, J. A., Laradji, M. (2009). Macromolecules, 42(3):803–810.

[21] Hernandez-Ortiz, J. P., Ma, H., de Pablo, J. J., Graham, M. D. (2006). Physics of Fluids, 18(12):123101 1–12. doi: http://dx.doi.org/10.1063/1.2397571.

[22] Kohale, S. C., Khare, R. (2009). The Journal of chemical physics, 130(10):104904 1–8.

[23] De Pablo, J. J., Öttinger, H. C., Rabin, Y. (1992). AIChE Journal, 38(2):273–283. ISSN 1547-5905. doi:10.1002/aic.690380213.

[24] Stavland, A. (2016). Private Communication.

[25] Hoogerbrugge, P. J., Koelman, J. M. V. A. (1992). Europhys. Lett., 19:155–160.

[26] Koelman, J. M. V. A., Hoogerbrugge, P. J. (1993). Europhys. Lett., 21:363–368.

[27] Kong, Y., Manke, C. W., Madden, W. G., Schlijper, A. G. (1994). Int. J. Thermophys., 15:1093–1101.

[28] Schlijper, A. G., Hoogerbrugge, P. J., Manke, C. W. (1995). J. Rheol., 39:567–579.

[29] Español, P., Warren, P. (1995). Europhys. Lett., 30:191–196.

[30] Swope, W. C., Andersen, H. C., Berens, P. H., Wilson, K. R. (1982). J. Cham. Phys., 76:648–649.

[31] Thijssen, J. M. (2007). Computational Physics. Cambridge University Press, second edition.

[32] Seaton, M. A., Anderson, R. L., Metz, S., Smith, W. (2013). Molec. Sim., 39:796–821.

[33] Doerr, T. P., Taylor, P. L. (1994). J. Chem. Phys., 101:10107–10117.

[34] Krafnick, R. C., García, A. E. (2015). The Journal of Chemical Physics, 143(24):243106 1–4.

[35] Gropp, W., Lusk, E., Skjellum, A. (1999). Using MPI: portable parallel programming with the message-passing interface. MIT Press, second edition.

[36] Träff, J. L., Benkner, S., Dongarra, J. J. (2012). Recent Advances in the Messsage Passing Interface. 19th European MPI Users' Group Meeting, EuroMPI 2012, Vienna, Austria, September 23-26, 2012. Proceedings. Springer.

[37] Pinches, M. R. R., Tildesley, D. J., Smith, W. (1991). Mol. Simul., 6:51–87.

[38] Brown, D., Clarke, J. H. R., Okuda, M., Yamazaki, T. (1994). Computer Physics Communications, 83(1):1 – 13.

[39] Plimpton, S. (1995). J. Comput. Phys., 117:1–19.

[40] Brown, D., Minoux, H., Maigret, B. (1997). Comp. Phys. Comm., 103:170–186.

[41] Plimpton, S., Pollock, R., Stevens, M. (1997). In Proceedings of the Eighth SIAM Conference on Parallel Processing for Scientific Computing. Minneapolis, MN.

[42] Sims, J. S., Martys, N. (2004). J. Res. Natl. Inst. Stand. Technol., 109:267–277.

[43] Steiner, T. (2009). Dissipative Particle Dynamics. Simulation of Microfluidic Systems With Fluid Particle Methods on High Performance Computers. Ph.D. thesis, University of Freiburg.

[44] Allen, M. P., Tildesley, D. J. (1987). Computer Simulation of Liquids. Oxford Science Publications.

[45] Revenga, M., Zuniga, I., Espanol, P., Pagonabarraga, I. (1998). International Journal of Modern Physics C, 09(08):1319–1328. doi: 10.1142/S0129183198001199.

[46] Liu, M., Meakin, P., Huang, H. (2007). Physics of Fluids, 19(3):033302 1–11. doi:http://dx.doi.org/10.1063/1.2717182.

[47] Finch, C. A. (1992). Polymer International, 28(3):256–256. ISSN 1097-0126. doi:10.1002/pi.4990280317.

[48] Chauveteau, G., Tirrell, M., Omari, A. (1984). Journal of Colloid and Interface Science, 100(1):41 – 54. ISSN 0021-9797. doi: http://dx.doi.org/10.1016/0021-9797(84)90410-7.

[49] Vinogradova, O. I. (1995). Langmuir, 11(6):2213–2220.

[50] Solomon, B. R., Khalil, K. S., Varanasi, K. K. (2014). Langmuir, 30(36):10970–10976. doi:10.1021/la5021143. PMID: 25144426.

[51] Bird, R., Dotson, P., Johnson, N. (1980). Journal of Non-Newtonian Fluid Mechanics, 7:213 – 235.

[52] Lindner, A., Vermant, J., Bonn, D. (2003). Physica A, 319:125 – 133.

[53] Herrchen, M., Ottinger, H. (1997). Journal of Non-Newtonian Fluid Mechanics, 68:17 – 42.

[54] Haward, S. J., Odell, J. A., Li, Z., Yuan, X.-F. (2010). Rheologica Acta, 49(7):781–788. ISSN 1435-1528. doi:10.1007/s00397-010-0453-x.